

Accepted manuscript

Richter, H. (2017) Mote3D: an open-source toolbox for modelling periodic random particulate microstructures, *Modelling and Simulation in Materials Science and Engineering*, Volume 25, Number 3, DOI: 10.1088/1361-651X/aa629a.

The outlined toolbox is available at <https://github.com/Mote3D>.

This is an author-created, un-copyedited version of an article accepted for publication/published in *Modelling and Simulation in Materials Science and Engineering*. IOP Publishing Ltd is not responsible for any errors or omissions in this version of the manuscript or any version derived from it. The Version of Record is available online at <https://doi.org/10.1088/1361-651X/aa629a>.

Mote3D: An open-source toolbox for modelling periodic random particulate microstructures

Henning Richter

Institute of Materials Research, German Aerospace Center (DLR), 51147 Cologne, Germany

E-mail: henning.richter@dlr.de

Abstract. The implementation of a comprehensive toolbox for generating microstructure models of periodic random particulate materials is outlined. The toolbox provides the functionality to create random configurations of overlapping or non-overlapping spherical particles with user-defined minimum inter-particle centre-to-centre distance and periodic boundary and export these random particle configurations for use in numerical simulations, either as lists of particle centre coordinates and radii or as Python-based scripts for generating solid geometric models or periodic hexahedral meshes ('voxel meshes'). The random particle configurations can be used as microstructure models to investigate or predict the microstructure-property relation of various engineering materials such as particle-reinforced composites, structural alloys, (partially-)sintered ceramics, powders, porous media or granular matter, as demonstrated by several examples. The outlined toolbox is open-source, giving users the possibility to modify and adapt the code to suit specific needs.

Keywords: particulate microstructure modelling, inhomogeneous materials, periodic boundary, numerical simulation

1. Introduction

With emerging scale-bridging simulation approaches, microstructure modelling has rapidly gained in importance in materials science and engineering. Detailed microstructure models provide a key tool for investigating the microstructure-property relation of current engineering materials and have successfully proven their potential for materials design and optimisation [1, 2, 3].

Microstructure model generation has to be robust and adaptable to a broad range of material microstructures and simulation approaches. Consequently, microstructure models are frequently created by combining simple geometric objects, which can conveniently be described by parametric equations, using Boolean operators. This approach permits computerization and yields models that provide adequate levels of detail to capture relevant microstructural characteristics.

The focus of the present paper is on the representation of random particulate microstructures. Both two- and three-dimensional particulate microstructure models have found wide application in materials science and engineering for the estimation of effective elastic [4, 5, 6, 7, 8], thermal [9, 10, 11], electrical [12, 13] and coupled

[14] material properties, for the numerical analysis of pore flow and permeability [15, 16], acoustical [17] and optical [18] characteristics, or for the simulation of powder compaction [19], particle sintering [20], metal forming [21] and additive manufacturing processes [22]. In this context, particulate models have been used to represent the microstructure of a diversity of materials such as alloys [17, 19, 21], metal matrix composites [9], polymer matrix composites [5, 14] or ceramics [4, 6, 23].

The present paper outlines the implementation and functionality of MOTe3D, a toolbox for the generation of three-dimensional models of random particulate microstructures. MOTe3D, which was written in GNU Octave [24], is open-source and platform-independent. User interaction with MOTe3D is realized through graphical user interfaces.

MOTe3D employs a modified Random Sequential Addition (RSA) scheme to generate random configurations of overlapping or non-overlapping spherical particles. It is worth noting that more powerful and efficient algorithms for positioning spherical particles are available [25, 26, 27]. An in-depth discussion on the characteristics of several algorithms can be found in Torquato (2002) [28]. However, the algorithm implemented in MOTe3D was chosen because it is robust and simple and, therefore, can be easily modified to suit user needs.

The paper is structured as follows: first, a brief description of the modelling approach underlying MOTe3D is given. Then, the implementation of MOTe3D as well as its relevant input parameters and output formats are explained. Finally, some examples are described to illustrate potential applications of MOTe3D.

2. Modelling approach

MOTe3D generates random particulate microstructure models with periodic boundary by randomly positioning spherical particles in a cubical computational domain. The algorithm underlying particle positioning is based on a modification of the classical Random Sequential Addition (RSA) scheme. For spheres in three-dimensional Euclidean space \mathbb{R}^3 , the classical RSA scheme was described by Widom [29]: within a predefined domain $\Omega \subseteq \mathbb{R}^3$, a random point \mathbf{p}_i that represents the centre of a sphere with radius r_i is generated. Then, at a second random point \mathbf{p}_j , another sphere with radius r_j is added. If the two spheres overlap, the position \mathbf{p}_j of the latter sphere is rejected and a new random point \mathbf{p}_k is generated. These attempts continue until the relation

$$\|\mathbf{p}_i - \mathbf{p}_k\| \geq (r_i + r_k) \quad (1)$$

is satisfied, i.e. the sphere with radius r_k can be placed inside the domain Ω without overlapping the previously positioned sphere with radius r_i . In a sequential process, additional random points are generated and further spheres are added without overlap until the predefined number n of spheres has been reached.

The classical RSA scheme represents a simple and robust approach to the generation

of random, non-clustered configurations of spheres. The resulting packing density η of the spheres, which is closely related to the porosity ϕ , is given by

$$\eta = \frac{1}{V_\Omega} \sum_{i=1}^n \frac{4}{3} \pi r_i^3 = 1 - \phi, \quad (2)$$

where V_Ω denotes the volume of the domain Ω . It is well known that, due to the random generation of potential sphere centres, the packing density η achievable by RSA is limited. Several studies have reported estimated packing density limits of around $\eta \approx 0.385$ or $\phi \approx 0.615$ for mono-sized spheres [27, 30, 31]. In practice, the achievable packing density depends on the number of positioning trials or execution time of the RSA computer implementation [27, 32]: with increasing numbers of successfully positioned spheres, the unoccupied space within Ω gets smaller, and the probability of finding admissible sphere positions decreases.

In order to be able to generate periodic particulate microstructure models covering a broad range of porosities ϕ within reasonable computational time, a modified RSA scheme was implemented in MOTÉ3D, the principal modifications being:

- the introduction of a predefined list of diameters from which the particle diameters are to be taken,
- the addition of the possibility to sort the list of diameters to assure that large particles are positioned first,
- the duplication of each sequentially generated particle protruding from the domain Ω to assure geometric periodicity of the resulting microstructure model,
- the additional translation of particle centres towards their nearest neighbour in order to slightly increase the packing efficiency and
- the admission of partial overlap between adjacent particles by introducing a particle overlap factor $0 < c \leq 1$, which defines the minimum acceptable distance between two particle centres, in order to reproduce the microstructure of (partially-)sintered particles or to create particle reinforcements for composite-type microstructures by selecting $c > 1$.

It is worth noting that these modifications to the classical RSA algorithm might introduce some bias with regard to the distribution of the particles in the resulting microstructure model. After model generation, it is therefore advisable to perform further statistical analyses in order to determine whether the generated microstructure model is an adequate representation of the material to be modelled.

In summary, the modified RSA algorithm yields a set \mathcal{P} of random position vectors \mathbf{p}_i , which mark the centres of n spherical particles with corresponding radii r_i ,

$$\mathcal{P} = \left\{ \mathbf{p}_i \in \mathbb{R}^3 \mid \|\mathbf{p}_i - \mathbf{p}_j\| \geq c(r_i + r_j); i, j = 1, \dots, n; i \neq j; c > 0 \right\}. \quad (3)$$

The minimum acceptable distance between any two adjacent particle centres in \mathcal{P} corresponds to c times the sum of their radii.

3. Implementation

3.1. Basic structure

The basic structure of the MOTE3D toolbox is shown in Fig. 1. Three main parts can be distinguished, namely the specification and generation of input parameters, the actual generation of the random particulate microstructure model and the export of the microstructure model. Each part and its core routines are outlined in the following sections.

3.2. Input parameter specification

After launching MOTE3D, the user is requested to specify the following input parameters via an input dialog box:

- the edge length of the cubical computational domain Ω ,
- the number n of spherical particles to be positioned within Ω ,
- the mean and the standard deviation of the particle diameter distribution,
- the particle overlap factor c that defines the minimum acceptable distance between adjacent particle centres,
- the maximum number of trials MOTE3D may make to position the n spherical particles within Ω ,
- an indication whether the list of particle diameters should be sorted,
- an indication whether graphical output of the generated microstructure is desired.

MOTE3D then generates a random distribution of particle diameters. By specifying the mean and standard deviation of the distribution, the diameters of the spherical particles can be controlled: setting the standard deviation equal to zero causes MOTE3D to create a list of n mono-sized particles, defining non-zero values for both the mean and standard deviation yields a list of n normally distributed particle diameters. With minor modification of the code it is also possible to import a list of particle diameters in order to realise skewed or multimodal particle diameter distributions, cf. Section 4.2.

During particle positioning, the values stored in the list of particle diameters are sequentially assigned to the randomly positioned particle centres in the domain Ω , as described in Section 2. The sorting option enables sorting of the list of particle diameters in descending order to assure that large particles are positioned first.

After completion of particle positioning, it is optionally possible to plot the resulting microstructure, as illustrated with the example shown in Fig. 2(a). It is, however, pointed out that the creation of such plots might be time-consuming for large numbers of particles.

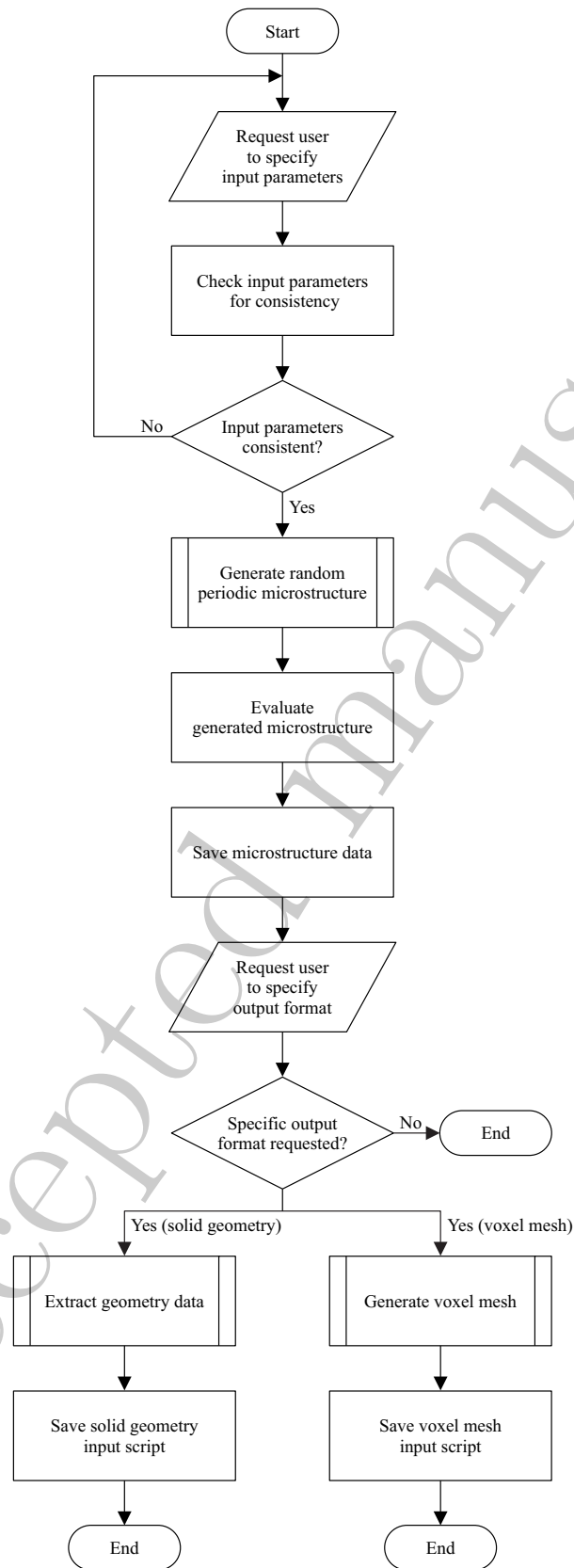


Figure 1: Flowchart of the process for generating random particulate microstructure models.

3.3. Microstructure model generation

To generate a random particulate microstructure model, the modified RSA scheme described in Section 2 is executed until the predefined number n of spherical particles has been placed inside the computational domain Ω or the maximum number of positioning trials has been reached. In the latter case, n will be updated with the actual number of successfully positioned particles.

Each particle addition requires the evaluation of the nearest-neighbour inter-particle centre-to-centre distances to check whether the newly added particle overlaps with any previously positioned particle. For mono-sized particles, the evaluation of the inter-particle centre-to-centre distances is straightforward, because only the distance between the newly added particle and its immediate neighbour is required: if the newly added particle does not overlap its immediate neighbour, it cannot overlap any other particle if all particles are of the same diameter. For particles with randomly distributed diameters, however, overlap might occur even if the centre-to-centre distance between the newly added particle and its immediate neighbour is sufficient. Consequently, in this case, the distances between the newly added particle and all surrounding particles have to be verified.

If an overlap larger than the predefined limit is detected between the newly added particle and a previously positioned particle, another random position is generated. If no overlap is found, or the overlap is below the predefined limit, the centre of the newly added particle is translated towards its nearest neighbour according to the particle overlap factor c . Additionally, a particle is placed on each vertex of Ω to facilitate the assignment of (periodic) boundary conditions for finite-element analyses.

After completion of particle positioning, the generated microstructure model is evaluated statistically with respect to the actual number n of successfully positioned particles, the mean and standard deviation of the actual particle diameter distribution and the minimum, maximum and mean nearest-neighbour inter-particle centre-to-centre distances. The coordinates of the particle centres and the corresponding particle radii are stored in the text files 'Positions.txt' and 'Radii.txt', respectively. The user-defined input parameters, as well as the statistical information about the generated microstructure model are reported in a text file named 'Statistics.txt'.

3.4. Microstructure model export

MOTÉ3D provides an export option that allows to use the generated particulate microstructure model with the commercial finite-element software Abaqus [33] or similar preprocessors. To this end, the model geometry is converted and stored as a Python-based [34] script readable by the Abaqus preprocessor. Two output formats are selectable by the user, as described in the following.

One possible choice is to export the generated microstructure model as geometry input script ('Abq_input_script.py'). If this script is executed in the Abaqus preprocessor, a solid geometric model of the microstructure is re-created by sequentially

generating the individual particles via revolution of the particles perimeter's sketch in the x-y-plane and re-positioning the particles according to their z-coordinate in the Abaqus assembly module, followed by merging of all particles to one part. Each particle is, by default, partitioned at three orthogonal planes to facilitate merging and meshing of the particles, however, this operation can be easily commented out in the input script. Particles that protrude from the predefined domain Ω are clipped respecting the requirement to preserve geometric periodicity in order to obtain a part with plane surfaces ready for mesh generation, cf. Fig. 2(b).

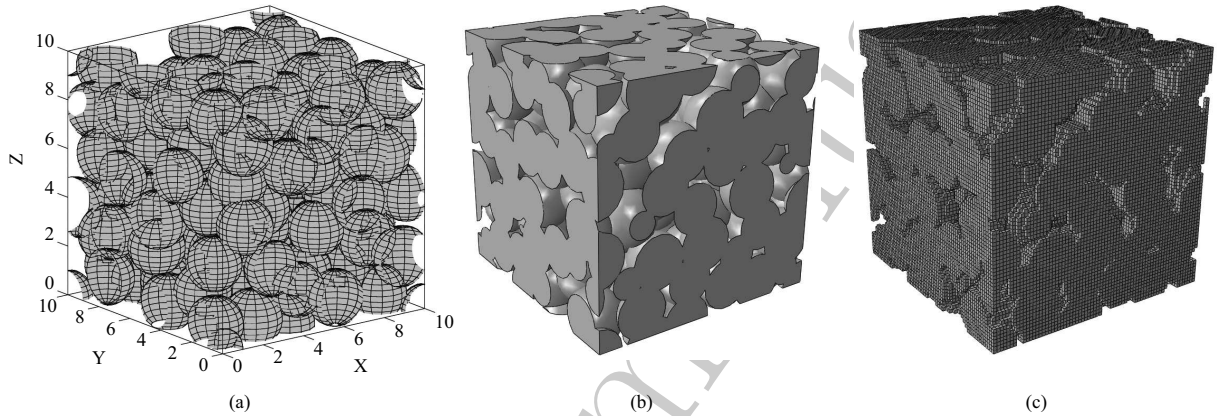


Figure 2: Exemplary periodic random microstructure model: (a) graphical output in MOTE3D, (b) solid geometric model of the microstructure in Abaqus and (c) voxel mesh consisting of 70^3 hexahedral elements.

Alternatively, the generated microstructure model can be exported as a periodic hexahedral mesh, a so-called ‘voxel mesh’, as exemplarily shown in Fig. 2(c). To this end, MOTE3D has a built-in grid-based mesh generator that sequentially discretises each spherical particle and creates a three-dimensional, boolean array of the computational domain Ω . In this three-dimensional array, the numbers of voxel elements representing the particles and the inter-particle space are stored separately. Both lists of element numbers are written to a voxel mesh input script (‘Abq_voxel_mesh.py’). By executing this script in the Abaqus preprocessor, the voxel mesh is re-created by re-assigning the element numbers to their respective positions within the discretised domain Ω . First- or second-order hexahedral elements with either reduced or full integration, i.e. Abaqus element types C3D8R, C3D8, C3D20R or C3D20 [33], can be user-selected.

The grid-based meshing approach is applicable to geometries that are too complex for conventional meshing with tetrahedral elements. It assures full periodicity of the resulting mesh, rendering it suitable for the application of periodic boundary conditions via nodal constraint equations. However, it has to be considered that the voxel mesh is an approximation of the true particle geometry, whose accuracy is strongly dependent on the element size, which can be manipulated by specifying the number of elements along each edge of the domain Ω . The effect of element size is discussed in Section 4.2.

4. Applications

4.1. Overview

In this section, three examples are given to demonstrate potential applications of MOTÉ3D. The first example covers the evaluation of the effective mechanical properties of an inhomogeneous three-phase material, i.e. a particle-reinforced composite containing spherical voids. The second example illustrates the modelling of second-phase particles in precipitation-hardened structural alloys. The third example focuses on the implementation of an analytical sintering model in order to generate microstructure models that resemble partially-sintered alumina particles.

4.2. Homogenization of elastic properties

4.2.1. Microstructure modelling Many technically relevant materials exhibit an inhomogeneous microstructure composed of constituents with different mechanical properties. In order to treat components made from such materials within the framework of continuum mechanics, the identification of the materials' effective mechanical properties, which are governed by volume fraction, shape, arrangement, interconnection and mechanical behaviour of the constituent phases, is required. Consequently, homogenization, i.e. the computation of the effective mechanical properties of inhomogeneous materials, is an important aspect of materials development and component design.

Existing analytical homogenization approaches are primarily aimed at ideally simple microstructures and fail to account for interactions between the stress and strain fields of adjacent inhomogeneities in materials with highly complex microstructure [35, 36, 37]. For such materials, numerical homogenization approaches generally yield improved estimates for the effective mechanical properties. In the following, the evaluation of the effective elastic moduli of a three-phase composite is outlined.

In this context, MOTÉ3D was used to generate a generic, periodic microstructure model representing a three-phase composite with randomly arranged particle reinforcements and a matrix phase containing several small spherical voids. To capture the size difference between particle reinforcements and voids, a list of bimodally distributed particle diameters was created by combining two sets of normally distributed random numbers with means 0.5 mm and 1.25 mm, respectively, and similar standard deviation of 0.1 mm. Fig. 3(a) shows a histogram of the resulting particle diameter distribution. The list of bimodally distributed particle diameters was imported to MOTÉ3D, and a random particle arrangement with particle overlap factor $c = 1.25$ was generated, cf. Fig. 3(b).

The particle arrangement was exported as voxel mesh, cf. Fig. 3(b), and the discretised microstructure model of the three-phase composite was then created in the Abaqus preprocessor: from the voxel mesh of a solid cube with 5 mm edge length, all elements associated with particles with diameters less than 1 mm were subtracted to

form small voids in the matrix domain. Those elements belonging to particles with diameters greater than 1 mm, i.e. a total of 30 of the 40 randomly positioned particles, were combined into one element set to constitute the particle reinforcement of the composite.

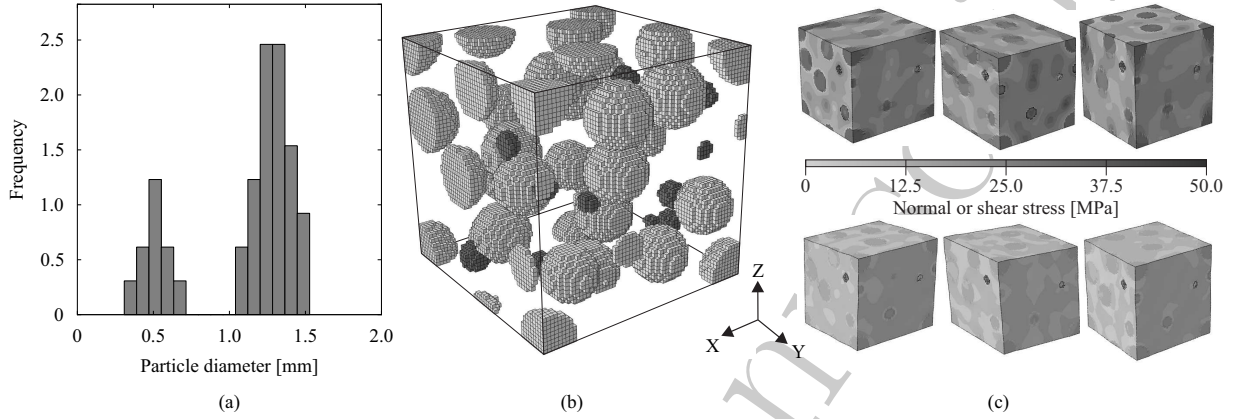


Figure 3: Microstructure model of a three-phase composite: (a) histogram of the bimodal particle diameter distribution imported to MOTÉ3D, (b) voxel mesh of the periodic random arrangement of particle reinforcements (light grey) and spherical voids (dark grey) and (c) deformation states (scaled by a factor of 100) and normal and shear stress distribution for the discretised model with 60^3 hexahedral elements (C3D20R) under the given strain component $\varepsilon_a = 0.001$.

In addition, the particle arrangement was exported as geometry input script and recreated in the Abaqus preprocessor. Using boolean operations, a solid geometric model of the three-phase composite microstructure was generated and automatically meshed with tetrahedral elements.

The three-phase composite microstructure model exhibits a particle volume fraction of approximately $\varphi_p = 17.5$ vol.% and a void volume fraction of $\varphi_v = 0.5$ vol.%. Arbitrary elastic properties were assigned to the constituent phases: for the matrix phase, Young's modulus $E_m = 10$ GPa and Poisson's ratio $\nu_m = 0.25$ were selected; for the particle reinforcement, the elastic parameters $E_p = 100$ GPa and $\nu_p = 0.25$ were used.

4.2.2. Numerical homogenization For the linearly elastic microstructure model domain Ω , the constitutive equation

$$\bar{\boldsymbol{\sigma}} = \bar{\mathbf{C}} : \bar{\boldsymbol{\varepsilon}}, \quad (4)$$

which relates the overall stress $\bar{\boldsymbol{\sigma}}$ and strain $\bar{\boldsymbol{\varepsilon}}$, has to be satisfied. In order to determine all entries of the unknown effective elasticity tensor $\bar{\mathbf{C}}$, the domain Ω was subjected to

six independent deformation states, i.e. three states of uniaxial strain

$$\bar{\boldsymbol{\varepsilon}}^{\text{I}} = \begin{bmatrix} \varepsilon_a & 0 & 0 \\ 0 & 0 & 0 \\ 0 & 0 & 0 \end{bmatrix}, \quad \bar{\boldsymbol{\varepsilon}}^{\text{II}} = \begin{bmatrix} 0 & 0 & 0 \\ 0 & \varepsilon_a & 0 \\ 0 & 0 & 0 \end{bmatrix}, \quad \bar{\boldsymbol{\varepsilon}}^{\text{III}} = \begin{bmatrix} 0 & 0 & 0 \\ 0 & 0 & 0 \\ 0 & 0 & \varepsilon_a \end{bmatrix}, \quad (5)$$

and three states of pure shear,

$$\bar{\boldsymbol{\varepsilon}}^{\text{IV}} = \begin{bmatrix} 0 & 0 & 0 \\ 0 & 0 & \frac{1}{2}\varepsilon_a \\ 0 & \frac{1}{2}\varepsilon_a & 0 \end{bmatrix}, \quad \bar{\boldsymbol{\varepsilon}}^{\text{V}} = \begin{bmatrix} 0 & 0 & \frac{1}{2}\varepsilon_a \\ 0 & 0 & 0 \\ \frac{1}{2}\varepsilon_a & 0 & 0 \end{bmatrix}, \quad \bar{\boldsymbol{\varepsilon}}^{\text{VI}} = \begin{bmatrix} 0 & \frac{1}{2}\varepsilon_a & 0 \\ \frac{1}{2}\varepsilon_a & 0 & 0 \\ 0 & 0 & 0 \end{bmatrix}, \quad (6)$$

with the arbitrary strain component ε_a [38]. For each deformation state, the resulting local stresses $\boldsymbol{\sigma}(\mathbf{x})$ were computed via the finite-element method, as shown in Fig. 3(c), assuming periodic boundary conditions [39]. The corresponding overall stress $\bar{\boldsymbol{\sigma}}$ was found by volume averaging the local stresses $\boldsymbol{\sigma}(\mathbf{x})$ in the domain Ω ,

$$\bar{\boldsymbol{\sigma}} = \frac{1}{V_\Omega} \int_\Omega \boldsymbol{\sigma}(\mathbf{x}) \, d\Omega \approx \frac{1}{V_\Omega} \sum_{i=1}^n \boldsymbol{\sigma}(\mathbf{x}_{\text{IP}_i}) V_{\text{IP}_i}, \quad (7)$$

which was realised by computing the weighted sum of the local stresses $\boldsymbol{\sigma}(\mathbf{x}_{\text{IP}_i})$ at n discrete integration points IP_i . In Eq. (7), V_Ω and V_{IP_i} denote the total volume of the domain Ω and the volume associated with integration point IP_i , respectively.

With the known strain and volume-averaged stress states $\bar{\boldsymbol{\varepsilon}}$ and $\bar{\boldsymbol{\sigma}}$, Eq. (4) can be solved for the effective elasticity tensor $\bar{\mathbf{C}}$. The effective elastic moduli can then be obtained from the overall compliance tensor $\bar{\mathbf{D}}$, which, in Voigt notation, reads

$$[\bar{\mathbf{D}}] = [\bar{\mathbf{C}}]^{-1} = \begin{bmatrix} \frac{1}{\bar{E}_1} & \frac{-\nu_{21}}{\bar{E}_2} & \frac{-\nu_{31}}{\bar{E}_3} & 0 & 0 & 0 \\ \frac{-\nu_{12}}{\bar{E}_1} & \frac{1}{\bar{E}_2} & \frac{-\nu_{32}}{\bar{E}_3} & 0 & 0 & 0 \\ \frac{-\nu_{13}}{\bar{E}_1} & \frac{-\nu_{23}}{\bar{E}_2} & \frac{1}{\bar{E}_3} & 0 & 0 & 0 \\ 0 & 0 & 0 & \frac{1}{G_{23}} & 0 & 0 \\ 0 & 0 & 0 & 0 & \frac{1}{G_{31}} & 0 \\ 0 & 0 & 0 & 0 & 0 & \frac{1}{G_{12}} \end{bmatrix} \quad (8)$$

for general orthotropic material behaviour. Overlines on the elastic constants denoting effective quantities have been omitted in Eq. (8) for better readability. The direction-dependent effective Young's moduli \bar{E}_i are related by

$$\frac{\bar{\nu}_{ij}}{\bar{E}_i} = \frac{\bar{\nu}_{ji}}{\bar{E}_j}, \quad (9)$$

where $\bar{\nu}_{ij}$ denotes the effective Poisson's ratio for transverse strain in j -direction under axial strain acting in i -direction.

4.2.3. *Homogenization results* Finite-element analyses of the three-phase composite microstructure model were performed using different element types and varying numbers of elements to study the convergence behaviour. The direction-dependent effective Young's moduli \bar{E}_1 , \bar{E}_2 and \bar{E}_3 obtained for regular voxel meshes with either first- or second-order hexahedral elements C3D8R, C3D20R or C3D20, and for boundary-conforming meshes with second-order tetrahedral elements C3D10, are plotted in Fig. 4. Periodic boundary conditions were realized via nodal constraint equations for opposite nodes of the regular voxel meshes, and by using surface-based tie constraints for the arbitrary, boundary-conforming meshes [40].

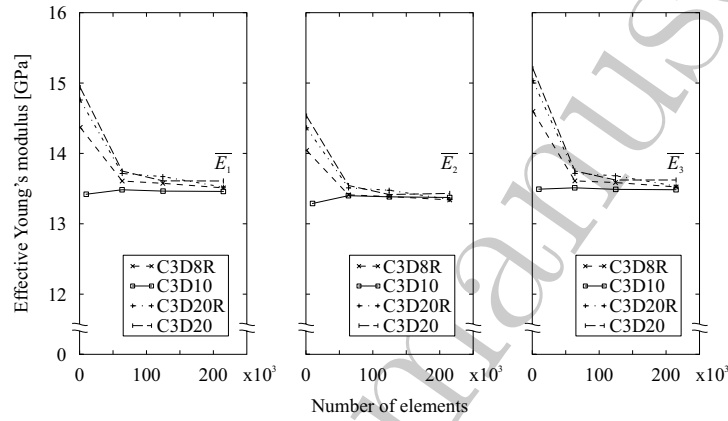


Figure 4: Effective Young's moduli \bar{E}_i obtained by numerical homogenization for different element types and various levels of mesh refinement.

The resulting effective Young's moduli \bar{E}_i are similar, indicating that the microstructure model exhibits approximately statistically isotropic behaviour. It can be observed that the effective Young's moduli converge fastest for the boundary-conforming meshes with second-order tetrahedral elements, and that coarse voxel representations tend to overestimate the effective Young's moduli. In the latter case, the results are largely unaffected by the voxel element type, which is attributable to the volume averaging of local stresses.

The plausibility of the results can be verified by a comparison with the Voigt (upper) bound,

$$\bar{E}_V = \sum_{i=1}^n \varphi_i E_i, \quad (10)$$

and the Reuss (lower) bound on the effective Young's modulus of a n -phase material,

$$\frac{1}{\bar{E}_R} = \sum_{i=1}^n \frac{\varphi_i}{E_i}, \quad (11)$$

where φ_i and E_i denote the volume fraction and the Young's modulus of the constituent phase i , respectively [41, 42]. While Eq. (10) yields $\bar{E}_V = 25.70$ GPa for the Voigt bound in the present case, due to the presence of voids with $E_v = 0$, the Reuss bound (as well

as the lower Hashin–Shtrikman bound) is equal to zero independent of void volume fraction [43]. However, neglecting the comparatively low volume fraction of voids in the present example, Eq. (11) yields $\bar{E}_R = 11.94$ GPa as an estimate for the lower bound. The computed effective Young’s moduli \bar{E}_i fall between the Voigt and estimated Reuss bounds.

Generally, in the presence of voids with vanishing elastic stiffness, the Voigt and Reuss bounds are too far apart to yield reliable results. In such cases, numerical homogenization of microstructure models leads to improved estimates for the effective elastic properties of multiphase composites.

4.3. Modelling of second-phase particles in structural alloys

To increase their strength, most structural alloys are precipitation-hardened, a treatment during which second-phase particles form. These second-phase particles hinder the movement of dislocations and affect strain localization and formability of the alloys [21].

This example illustrates how MOTÉ3D can be used to model second-phase particles. In order to generate an unbiased random configuration of second-phase particles, no minimum acceptable distance between adjacent particle centres was specified and any additional translation of particle centres towards their nearest neighbour was deactivated in MOTÉ3D. In addition, geometric periodicity was not accounted for, i.e. only the particle centre coordinates and radii stored in the text files ‘Positions.txt’ and ‘Radii.txt’ were used to re-create the solid geometric model of the second-phase particles. An exemplary microstructure model of a bi-crystal section with 100 second-phase particles is shown in Fig. 5(b). The model was generated using boolean operations. Due to the pronounced difference in size between the second-phase particles and the crystallites, only a small section of the bi-crystal with 2 μm edge length was modelled. The mean and standard deviation of the second-phase particles’ diameter distribution were 0.2 μm and 0.02 μm , respectively.

The statistical properties of the random configuration of second-phase particles can be easily evaluated using the lists of particle centre coordinates and radii. As an example, the distribution of nearest-neighbour inter-particle centre-to-centre distances is plotted in Fig. 5(a).

The solid geometric model of the bi-crystal section exhibits comparatively low complexity and can be discretized using automatic mesh generation in Abaqus. The resulting mesh of the bi-crystal section consisting of approximately 500 000 tetrahedral elements is shown in Fig. 5(c).

4.4. Implementation of a sintering model

4.4.1. Analytical sintering model The mechanical properties of a partially-sintered, porous ceramic body are governed by the geometry of the sintering necks between adjacent ceramic particles [44, 45, 46, 47, 48]. Consequently, a numerical model

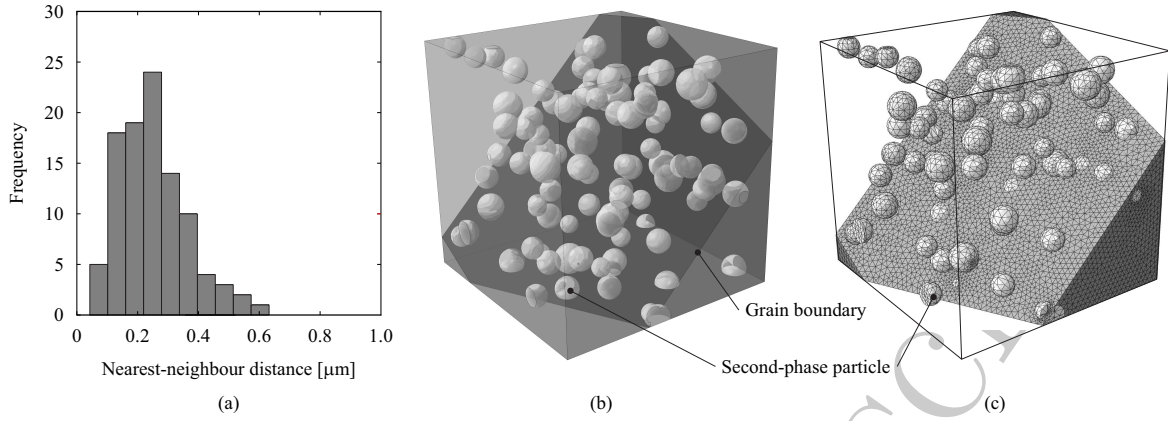


Figure 5: Modelling of second-phase particles in precipitation-hardened structural alloys: (a) distribution of nearest-neighbour inter-particle centre-to-centre distances, (b) exemplary bi-crystal section with 100 second-phase particles and (c) mesh of the bi-crystal section.

intended to realistically represent the microstructure of a partially-sintered ceramic body has to account for this essential characteristic. Microstructure models described in literature, however, are generally based on random arrangements of spherical particles with arbitrarily chosen overlap and irregular sintering neck geometry [23, 6]. In the following, a novel approach is presented, which combines an analytical sintering model with MOTE3D to yield an improved representation of the actual contact surfaces and distances between adjacent, partially-sintered, mono-disperse alumina particles.

In general, sintering is a highly complex process involving different mechanisms of material transport. Various analytical models have been proposed in literature to describe these mechanisms for a simplified two-particle configuration [49, 50, 51, 52]. This example solely focusses on volume diffusion, an important mechanism of material transport during the initial stage of solid-state sintering of alumina, which leads to sintering neck growth and densification [50]. The resulting sintering neck geometry can be replicated by properly adjusting the centre-to-centre distance of two ideally spherical alumina particles [53], as schematically shown in Fig. 6(a).

The dependence of the sintering neck size on sintering time is commonly described by a power law of the form

$$\left(\frac{s}{r}\right)^v = \frac{A}{r^w} t, \quad (12)$$

where s and r are the sintering neck radius and the particle radius, respectively, and t denotes the sintering time. The constant A and the exponents v and w depend on the type of diffusion process [49, 50, 51, 52]. For volume diffusion between the grain boundary and the sintering neck region, Kingery and Berg derived a relation for A and suggested the exponents $v = 5$ and $w = 3$ [49]. Coble adapted this relation to the

two-particle configuration and obtained

$$A = \frac{960 D_v \gamma \delta^3}{kT}, \quad (13)$$

where D_v is the apparent volume diffusion coefficient, γ is the surface energy, δ^3 is the vacancy volume, k is the Boltzmann constant and T is the absolute temperature [50]. From experiments on the shrinkage of compacts of alumina particles with mean radius $r = 0.1 \mu\text{m}$ after sintering at $T = 1573.15 \text{ K}$, Coble found an apparent volume diffusion coefficient of $D_v = 1.3 \cdot 10^{-20} \text{ m}^2/\text{s}$ for $\gamma = 1 \text{ J/m}^2$ and $\delta^3 = 1.4 \cdot 10^{-29} \text{ m}^3$ [50].

4.4.2. Computation of sintering neck size The analytical sintering model can be used to determine a time- and temperature-dependent particle overlap factor c . Relating the sintering neck radius s to the particles' centre-to-centre distance leads to the expression

$$c = \sqrt{1 - \left(\frac{s}{r}\right)^2}, \quad (14)$$

which can be solved for a given particle radius r . For mono-disperse alumina particles with $r = 0.1 \mu\text{m}$ sintered at $T = 1573.15 \text{ K}$, the dependence of c on sintering time t is plotted in Fig. 6(b). To illustrate the effect of a variation in c , cross-sections of exemplary microstructure models with particle overlap factors corresponding to sintering times of $t = 1 \text{ min}$, 10 min and 100 min are shown in Fig. 6(c). For such small particle overlap factors, additional translation of particle centres towards their nearest neighbour minimises the occurrence of 'loose' particles within the model domain.

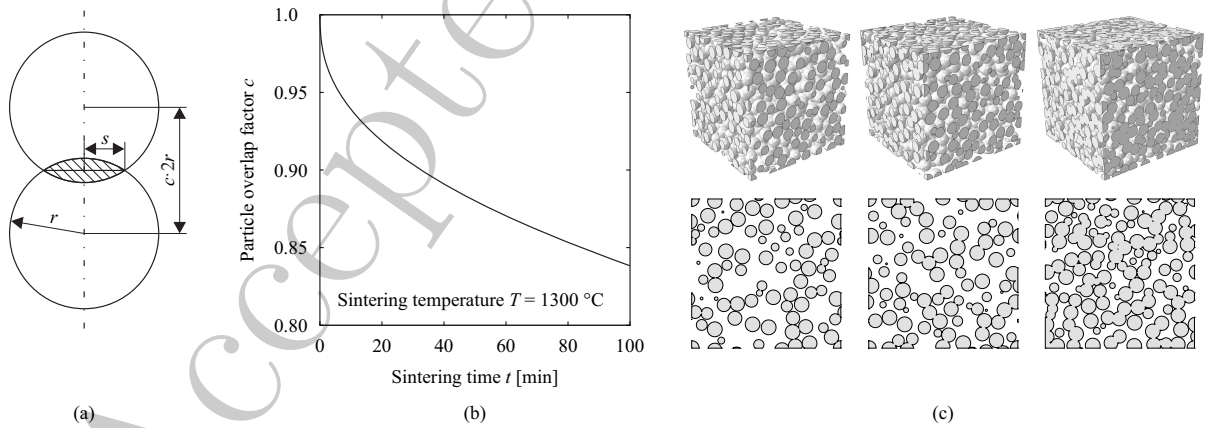


Figure 6: Implementation of a sintering model for partially-sintered alumina: (a) geometry of two-particle model, (b) dependence of the particle overlap factor c on sintering time t and (c) exemplary microstructure models of partially-sintered alumina particles ($r = 0.1 \mu\text{m}$) with particle overlap factors corresponding to sintering times of $t = 1 \text{ min}$, 10 min and 100 min at $1300 \text{ }^\circ\text{C}$.

It is pointed out that the described approach is not intended to simulate the sintering process in detail, but to replicate the geometry of (partially-)sintered particles. It can also be applied to poly-disperse particle distributions if the differences in particle

sizes are not too large. In this case, an equivalent average radius can be computed for each particle pair [54, 55].

5. Summary

In the present paper, the implementation and functionality of MOTe3D, an open-source toolbox for modelling periodic random particulate microstructures, have been described. The random configurations of overlapping or non-overlapping spherical particles generated by MOTe3D can be used to represent the microstructure of various engineering materials, as demonstrated by several examples.

The random configurations of particles generated by MOTe3D can be exported as Python-based scripts, which are readable by the Abaqus preprocessor. Thus, either solid geometric models or periodic voxel meshes of the microstructures can be directly re-created in Abaqus for numerical simulations. Alternatively, the random particle configurations can be stored as lists containing the coordinates and radii of the particles, which can serve as input for molecular dynamics or discrete element simulations.

MOTe3D is open-source and licensed under the GNU General Public License [56], giving users the possibility to easily modify, adapt or extend the code to suit specific needs.

6. Acknowledgements

MOTe3D is available at: https://github.com/Mote3D/Mote3D_toolbox. Fruitful discussions with M.R. Kabir on the microstructure modelling of structural alloys are gratefully acknowledged.

References

- [1] Janssens K G F, Raabe D, Kozeschnik E, Miodownik M A and Nestler B 2007 *Computational Materials Engineering* (Burlington: Academic Press)
- [2] Ghosh S and Dimiduk D 2010 *Computational Methods for Microstructure-Property Relationships* (Berlin, Heidelberg: Springer)
- [3] Horstemeyer M F 2012 *Integrated Computational Materials Engineering (ICME) for Metals* (New Jersey: Wiley & Sons)
- [4] Roberts A P and Garboczi E J 2000 Elastic Properties of Model Porous Ceramics *J. Am. Ceram. Soc.* **83** 3041–48
- [5] Segurado J and Llorca J 2002 A numerical approximation to the elastic properties of sphere-reinforced composites *J. Mech. Phys. Solids* **50** 2107–21
- [6] Jauffrès D, Martin C L, Lichtner A and Bordia R K 2012 Simulation of the elastic properties of porous ceramics with realistic microstructure *Modelling Simul. Mater. Sci. Eng.* **20** 045009-1–18
- [7] Richter H 2015 Homogenisation of porous thin films and perforated layers: Comparison of analytical and numerical approaches *Mech. Mater.* **89** 119–29
- [8] Schneider M, Merkert D and Kabel M 2016 FFT-based homogenization for microstructures discretized by linear hexahedral elements *Int. J. Numer. Meth. Eng.* **2016**
- [9] Davis L C and Artz B E 1995 Thermal conductivity of metal-matrix composites *J. Appl. Phys.* **77** 4954–60

- [10] Argento C and Bouvard D 1996 Modeling the effective thermal conductivity of random packing of spheres through densification *Int. J. Heat Mass Transfer* **39** 1343–50
- [11] Zhang H W, Zhou Q, Xing H L, and Muhlhaus H. 2011 A DEM study on the effective thermal conductivity of granular assemblies *Powder Technol.* **205** 172–83
- [12] Chan Kim I and Torquato S 1991 Effective conductivity of suspensions of hard spheres by Brownian motion simulation *J. Appl. Phys.* **69** 2280–89
- [13] Rhazaoui K, Cai Q, Kishimoto M, Tariq F, Somalu M R, Adjiman C S and Brandon N P 2015 Towards the 3D Modelling of the Effective Conductivity of Solid Oxide Fuel Cell Electrodes - Validation against experimental measurements and prediction of electrochemical performance *Electrochim. Acta* **168** 139–47
- [14] Miehe C, Vallicotti D and Teichtmeister S 2016 Homogenization and multiscale stability analysis in finite magneto-electro-elasticity. Application to soft matter EE, ME and MEE composites *Comput. Methods in Appl. Mech. Eng.* **300** 294–346
- [15] Vidal D, Ridgway C, Pianet G, Schoelkopf J, Roy R and Bertrand F 2009 Effect of particle size distribution and packing compression on fluid permeability as predicted by lattice-Boltzmann simulations *Comput. Chem. Eng.* **33** 256–66
- [16] Garcia X, Akanji L T, Blunt M J, Matthai S K and Latham J P 2009 Numerical study of the effects of particle shape and polydispersity on permeability *Phys. Rev. E* **80** 021304-1–9
- [17] Janousch C, Winkler R, Wiegmann A, Pannert W, Merkel M and Öchsner A 2014 Simulation and experimental validation of acoustic properties of hollow sphere structures *Mat.-wiss. u. Werkstofftech.* **45** 413–22
- [18] Zohdi T I 2006 On the optical thickness of disordered particulate media *Mech. Mater.* **38** 969–81
- [19] Harthong B, Jérrier J-F, Dorémus P, Imbault D and Donzé F-V 2009 Modeling of high-density compaction of granular materials by the Discrete Element Method *Int. J. Solids Struct.* **46** 3357–64
- [20] Bodla K K and Garimella S V 2014 Simulated Microstructural Evolution and Design of Porous Sintered Wicks *J. Heat Transfer* **136** 072601-1–10
- [21] Inal K, Simha H M and Mishra R K 2008 Numerical Modeling of Second-Phase Particle Effects on Localized Deformation *J. Eng. Mater. Technol.* **130** 021003-1–8
- [22] Khairallah S A and Anderson A 2014 Mesoscopic simulation model of selective laser melting of stainless steel powder *J. Mater. Process. Technol.* **214** 2627–36
- [23] Bruno G, Efremov A M, Levandovskiy A N and Clausen B 2011 Connecting the macro- and microstrain responses in technical porous ceramics: modeling and experimental validations *J. Mater. Sci.* **46** 161–73
- [24] Eaton J W, Bateman D, Hauberg S and Wehbring R 2015 *GNU Octave version 4.0.0 manual: a high-level interactive language for numerical computations*
- [25] Lubachevsky B D and Stillinger F H 1990 Geometric properties of random disk packings *J. Stat. Phys.* **60** 561–83
- [26] Torquato S, Uche O U and Stillinger F H 2006 Random sequential addition of hard spheres in high Euclidean dimensions *Phys. Rev. E* **74** 061308-1–16
- [27] Zhang G and Torquato S 2013 Precise algorithm to generate random sequential addition of hard hyperspheres at saturation *Phys. Rev. E* **88** 053312-1–9
- [28] Torquato S 2002 *Random heterogeneous materials: microstructure and macroscopic properties* (New York: Springer)
- [29] Widom B. 1966 Random Sequential Addition of Hard Spheres to a Volume *J. Chem. Phys.* **44** 3888–94
- [30] Cooper D W 1988 Random-sequential-packing simulations in three dimensions for spheres *Phys. Rev. A* **38** 522–4
- [31] Talbot J, Schaaf P and Tarjus G 1991 Random sequential addition of hard spheres *Mol. Phys.* **72** 1397–406
- [32] Feder J 1980 Random sequential adsorption *J. Theor. Biol.* **87** 237–54

- [33] Dassault Systèmes 2010 *Abaqus*[®] FEA 6.10
- [34] van Rossum G and de Boer J 1991 Interactively Testing Remote Servers Using the Python Programming Language *CWI Quarterly* **4** 283–303
- [35] Christensen R 1990 A critical evaluation for a class of micro-mechanics models *J. Mech. Phys. Solids* **38** 379–404
- [36] Christensen R, Schantz H and Shapiro J 1992 On the range of validity of the Mori-Tanaka method *J. Mech. Phys. Solids* **40** 69–73
- [37] Zheng Q-S and Du D-X 2001 An explicit and universally applicable estimate for the effective properties of multiphase composites which accounts for inclusion distribution, *J. Mech. Phys. Solids* **49** 2765–88
- [38] Zohdi T I and Wriggers P 2005 *An Introduction to Computational Micromechanics* (Berlin, Heidelberg: Springer)
- [39] Michel J, Moulinec H and Suquet P 1999 Effective properties of composite materials with periodic microstructure: a computational approach *Comput. Methods Appl. Mech. Engrg.* **172** 109–43
- [40] Yuan Z and Fish J 2008 Toward realization of computational homogenization in practice *Int. J. Numer. Meth. Eng.* **73** 361–80
- [41] Voigt W 1889 Ueber die Beziehung zwischen den beiden Elasticitätsconstanten isotroper Körper *Ann. Phys.* **274** 573–87
- [42] Reuss A 1929 Berechnung der Fließgrenze von Mischkristallen auf Grund der Plastizitätsbedingung für Einkristalle *Z. Angew. Math. Mech.* **9** 49–58
- [43] Norris A N 1985 A differential scheme for the effective moduli of composites *Mech. Mater.* **4** 1–16
- [44] Lam D C C, Lange F F and Evans A G 1994 Mechanical Properties of Partially Dense Alumina Produced from Powder Compacts *J. Am. Ceram. Soc.* **77** 2113–7
- [45] Arató P, Besenyi E, Kele A and Wéber F 1995 Mechanical properties in the initial stage of sintering *J. Mater. Sci.* **30** 1863–71
- [46] Hardy D and Green D J 1995 Mechanical properties of a partially sintered alumina *J. Eur. Ceram. Soc.* **15** 769–75
- [47] Rice R W 1996 Evaluation and extension of physical property-porosity models based on minimum solid area *J. Mater. Sci.* **31** 102–18
- [48] Ohji T and Fukushima M 2012 Macro-porous ceramics: processing and properties *Int. Mater. Rev.* **57** 115–31
- [49] Kingery W D and Berg M 1955 Study of the Initial Stages of Sintering Solids by Viscous Flow, Evaporation-Condensation, and Self-Diffusion *J. Appl. Phys.* **26** 1205–12
- [50] Coble R L 1958 Initial Sintering of Alumina and Hematite *J. Am. Ceram. Soc.* **41** 55–62
- [51] Johnson D L and Cutler I B 1963 Diffusion Sintering: I, Initial Stage Sintering Models and Their Application to Shrinkage of Powder Compacts *J. Am. Ceram. Soc.* **46** 541–5
- [52] Exner H E 1978 *Grundlagen von Sintervorgängen* (Berlin, Stuttgart: Borntraeger)
- [53] Richter H 2012 *Multiscale homogenization of ceramic composites with porous matrix phase* (Bochum University, Ph.d. thesis)
- [54] Pan J, Le H, Kucherenko S and Yeomans J A 1998 A model for the sintering of spherical particles of different sizes by solid state diffusion *Acta Mater.* **46** 4671–90
- [55] Maximenko A L, Van Der Biest O and Olevsky E A 2003 Prediction of initial shape of functionally graded ceramic pre-forms for near-net-shape sintering *Sci. Sinter.* **35** 5–12
- [56] Free Software Foundation 2007 *GNU General Public License* <http://www.gnu.org/licenses/gpl-3.0.html>